Study of low temperature effect on the fracture locus of a 420 MPa structural steel with the edge tracing method

S. Tu[1], X. Ren[2], T. A. Kristensen[2], J. He[1], Z. Zhang[1,*]

[1]Department of Structural Engineering, Norwegian University of Science and Technology, Trondheim 7491, Norway

[2]SINTEF Materials and Chemistry, Trondheim 7456, Norway

Highlights

- Low temperature effect on the fracture locus of a structural steel has been investigated.
- A two-plane mirror system was designed to capture specimen deformation.
- The edge tracing method was used to measure specimen deformation.
- It shows that low temperature effect (down to -60℃) on fracture locus is insignificant.

* Corresponding author: Tel: +47 73592530
E-mail address: zhiliang.zhang@ntnu.no (Z. Zhang)
Fax: +47 73594700

Nomenclature

a	current minimum cross-section radius
a_0	initial minimum cross-section radius
A	current minimum cross-section area
A_0	initial minimum cross-section area
D	material failure indictor
E	Young's modulus
L	Lode parameter
R	current notch curvature radius
R_0	initial notch curvature radius
a/R	current notch radius ratio
a_0/R_0	initial notch radius ratio
T	stress triaxiality
T^*	strain-averaged stress triaxiality
v	Poisson's ratio
ε	average true strain
ε_f	fracture strain
$\varepsilon_{P_{\max}}$	strain at the maximum load
σ_1, σ_2, σ_3	the first, second and third principle stress
σ_{eq}	Mises equivalent stress
σ_m	hydrostatic stress
σ_t	true stress

Study of low temperature effect on the fracture locus of a 420 MPa structural steel with the edge tracing method

S. Tu[1], X. Ren[2], T. A. Kristensen[2], J. He[1], Z. Zhang [1,*]

[1]Department of Structural Engineering, Norwegian University of Science and Technology, Trondheim 7491, Norway

[2]SINTEF Materials and Chemistry, Trondheim 7456, Norway

Abstract

Quasi-static tensile tests with smooth round bar and axisymmetric notched tensile specimens have been performed to study the low temperature effect on the fracture locus of a 420 MPa structural steel. Combined with a digital high-speed camera and a two-plane mirrors system, specimen deformation was recorded in two orthogonal planes. Pictures taken were then analyzed with the edge tracing method to calculate the minimum cross-section diameter reduction of the necked/notched specimen. Obvious temperature effect was observed on the load-strain curves for smooth and notched specimens. Both the strength and strain hardening characterized by the strain at maximum load increase with temperature decrease down to -60℃. Somewhat unexpected, the fracture strains (ductility) of both smooth and notched specimens at temperatures down to -60℃ do not deteriorate, compared with those at room temperature. Combined with numerical analyses, it shows that the effect of low temperatures (down to -60℃) on fracture locus is insignificant. These findings shed new light on material selection for Arctic operation.

Keywords: *fracture locus; low temperature; notched tensile specimen; edge tracing method; stress triaxiality.*

1. Introduction

The increasing demands of energy motivate the petroleum sector to move their exploitation activities to harsher environments, resulting in new challenges for structural design, maintenance, and failure assessment. It has been demonstrated that there are considerable oil and gas resources in the Arctic region [1], the low temperature effect should be considered in the selection of structural steels. Previous research has shown that decreasing temperature increases the yield strength of most steels. Ren [2] carried out tensile tests of a 420 MPa steel with temperature ranging from 0℃ down to -90℃, and found that the Lüders strain [3-5] increased as the temperature decreased. For most structural steels, as the temperature decreases continuously, the fracture behavior will transform from ductile to brittle (DBT) [6-12], reducing the steels' ductility and fracture toughness. The DBT occurs when the temperature decreases down to the steel's DBT temperature.

Hybrid experimental-numerical analyses [13-18] or numerical analyses with unit cell model [19, 20] alone have demonstrated that the fracture strain ε_f (the equivalent strain corresponding to crack initiation) strongly depends on the stress triaxiality and the Lode angle parameter. The stress triaxiality T which is defined by the ratio of the mean stress σ_m and the von Mises equivalent stress σ_{eq} ($T = \sigma_m / \sigma_{eq}$) is widely used to characterize the hydrostatic pressure effect [21-25] and crack tip constraint level [26-28]. Bao [13] carried out a series of tests on 2024-T351 aluminum alloy with initial stress triaxiality ranging from -0.33 to 1 at room temperature. Combined with numerical analyses, a fracture strain versus strain-weighted average stress triaxiality T^* diagram was established. The curve, namely the fracture locus consists of three branches: the fracture strain decreases with the increase of T^* when $-0.33 < T^* < 0$ and $T^* > 0.33$; while the fracture strain increases in the range $0 \le T^* \le 0.33$. Recent study shows that the Lode angle parameter L ($L = (2\sigma_2 - \sigma_1 - \sigma_3)/(\sigma_1 - \sigma_3)$; σ_1, σ_2, σ_3 are the principle stresses) also plays an important role on the evolution of fracture locus [16, 19, 29-32]. For smooth round bar and axisymmetric notched specimens under quasi-static tensile loading, which are the focus of this study, the Lode angle parameter at a given material point on the minimum cross-section is constant [32, 33], and therefore will not be discussed here. The influence of loading rate [18, 22], loading path [19, 20, 31, 34] on the evolution of the fracture locus have been studied extensively in the range of the stress triaxiality $T > 0.33$. Johnson and Cook [22] performed torsion tests over a range of strain rates, Hopkinson bar tests over a range of temperatures and quasi-static tensile tests with various notch geometries to investigate fracture characteristics of OFHC copper, Armco iron and 4340 steel. Their test results indicate that fracture strain is very dependent on stress triaxiality and less dependent on strain rate and temperature. Hopperstad and Børvik [18, 35, 36] performed Split Hopkinson tension tests on the structural steel Weldox 460E at high strain rates and elevated temperatures (100 to 500℃) with smooth and axisymmetric notched specimens, neither obvious strain rate effect nor temperature dependence on the fracture locus was observed.

Fracture locus of metallic materials has attracted wide attention over the past decades, however, the study on the effect of low temperature on fracture locus is very limited. In order to facilitate the selection of structural steels for the application in the Arctic region, it is very important to characterize the low temperature effect on fracture locus of structural steels.

In the current study, we carried out quasi-static tensile tests with smooth and axisymmetric notched specimens made of a 420 MPa structural steel, with temperature varied from room temperature down to -60℃. A digital high-speed camera was used to record the specimen deformation during the test in conjunction with a two-plane mirrors system. Pictures taken were then analyzed with the edge tracing method to calculate the global average strain, up to crack initiation. Detailed information about the test

materials, test set-up and the edge tracing method are introduced in section 2. Experimental results are presented in section 3. Numerical analyses are performed to simulate the experiments to capture the stress triaxiality evolution at the location where crack initiation is supposed to occur. The numerical procedure and results are presented in section 4. The results indicate that both the strength and hardening characterized by the strain at maximum load increase with the decrease of temperature, while the temperature down to -60℃ does not significantly alter the dependence of fracture strain on stress triaxiality.

2. Experimental program

2.1 Material and specimens

The specimens were machined from 50 mm thick plates of a 420 MPa steel, along the rolling direction. Sketches of the smooth round bar specimens and axisymmetric notched tensile specimens are shown in Fig. 1. Bridgman [21] proposed an analytic solution to characterize the stress distribution of a necked tensile specimen, the stress triaxiality in the center of the minimum cross section where crack formation occurs first is expressed as:

$$T = \frac{1}{3} + \ln(1 + \frac{a}{2R}) \tag{1}$$

where a and R are the current minimum cross-section radius and the notch curvature radius of a necked tensile specimen, respectively. Bao performed tensile test with smooth round bar specimen numerically, and found that the stress distribution differed significantly with Bridgman's analytical solution on the minimum cross-section. Based on numerical simulation, an empirical expression of stress triaxiality in the center of specimen minimum cross-section was proposed [33, 37]:

$$T = \frac{1}{3} + \sqrt{2}\ln(1 + \frac{a}{2R}) \tag{2}$$

According to Eq. (1) and Eq. (2), the stress triaxiality in the center of specimen minimum cross-section is a function of the notch radius ratio a/R. By machining axisymmetric notch in the center of smooth specimen, different initial stress triaxiality can be realized by varying the initial notch radius ratio, a_0/R_0. For all the axisymmetric notched specimens tested in present study, $a_0 = 6\,\text{mm}$. a_0/R_0 varied from 0.5 to 3 by varying R_0 from 2 mm to 12 mm. Combined with the smooth round bar specimen, the initial stress triaxiality varied in a range from 0.33 to 1.63, calculated by Eq. (2).

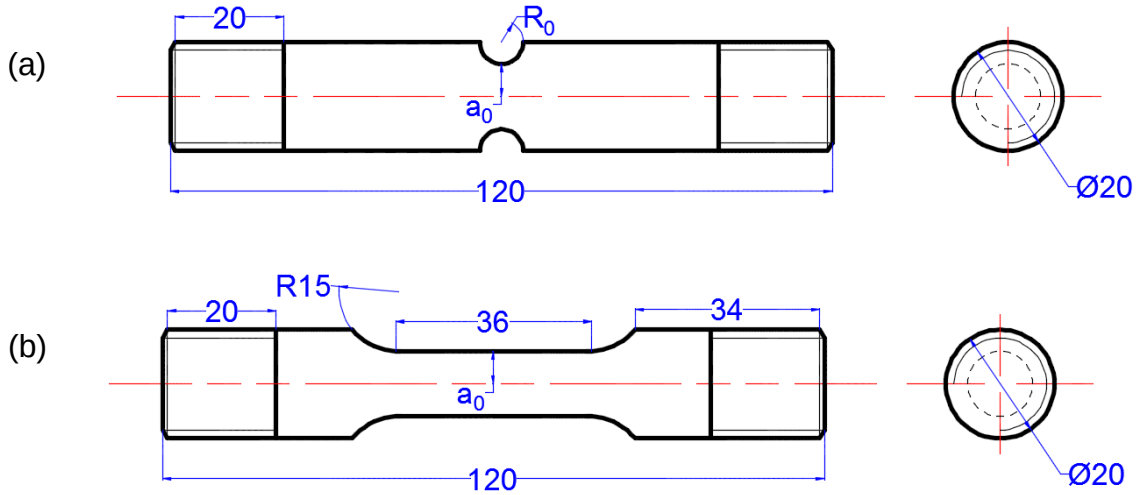

Fig. 1 Sketches of the tensile Specimens: (a) axisymmetric notched tensile specimen; (b) smooth round bar specimen.

2.2 Test set-up

The test set-up is shown in Fig. 2. The tests were carried out using an universal test machine **Instron 5985,** with the loading cell of 250 KN. A liquid nitrogen-cooled temperature chamber was used to create low temperature environment. The tests were carried out at room temperature, -30℃, and -60℃. The air inside of the temperature chamber was replaced with nitrogen gas first, in order to avoid ice formation on the specimen surface. A thermocouple shown in Fig. 3 (a) was used to measure the temperature at the specimen surface. On one side of the temperature chamber, there is a window, through which the inside of the temperature chamber can be observed clearly. A digital high-speed CCD camera with the resolution of 2448×2050 pixels was located besides the window to take pictures of the specimen during the test, with the framing rate of 1 frame per second. All the tests were performed in displacement control manner, with the crosshead speed of 0.3 mm/minute. During the tests, the force was recorded with the same camera framing frequency

Inside the temperature chamber, there are two LED lights and a two-plane mirrors system, as seen in Fig. 3. The two-plane mirrors system consists of 2 plane mirrors with the angle of 135°, as illustrated in Fig. 3 (b). The specimen and the camera located on the angle bisector of the two-plane mirrors system. According to the plane image formation principle, the specimen images form in two orthogonal planes, seen in Fig. 3 (b). Therefore, the deformation of the specimen can be observed in two perpendicular directions during the test. The consideration of using the two-plane mirrors system is that, due to the localized deformation on necked smooth and axisymmetric notched specimens, it is more accurate to use the average value of minimum cross-section diameter in two orthogonal directions to calculate the current minimum cross-section area, instead of only one direction [36]. By adjusting the position of the LED lights, the specimen images can be located in the LED light images center. The camera was set in

mono mode in the test. A very strong grey-value gradient can be formed between the specimen images and the picture background, for the purpose to use the edge tracing method to measure the specimen deformation. Fig. 4 shows a picture of a smooth specimen taken with the camera in the beginning of the test.

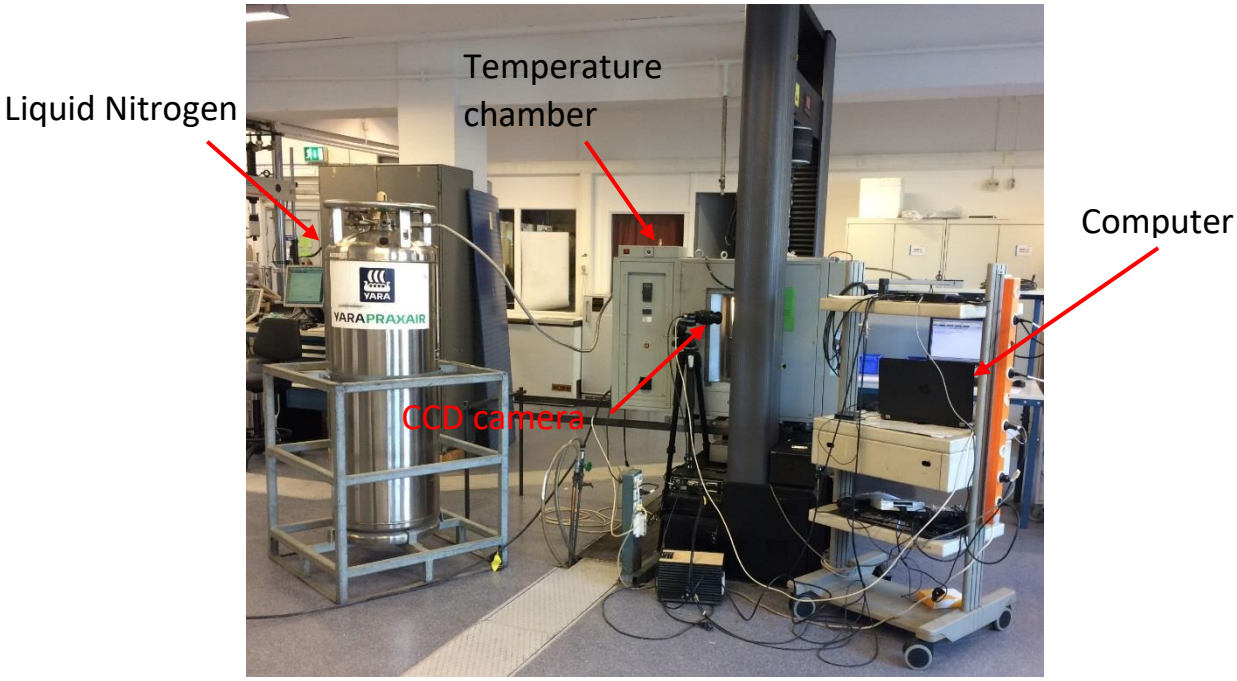

Fig. 2 Test system in this study

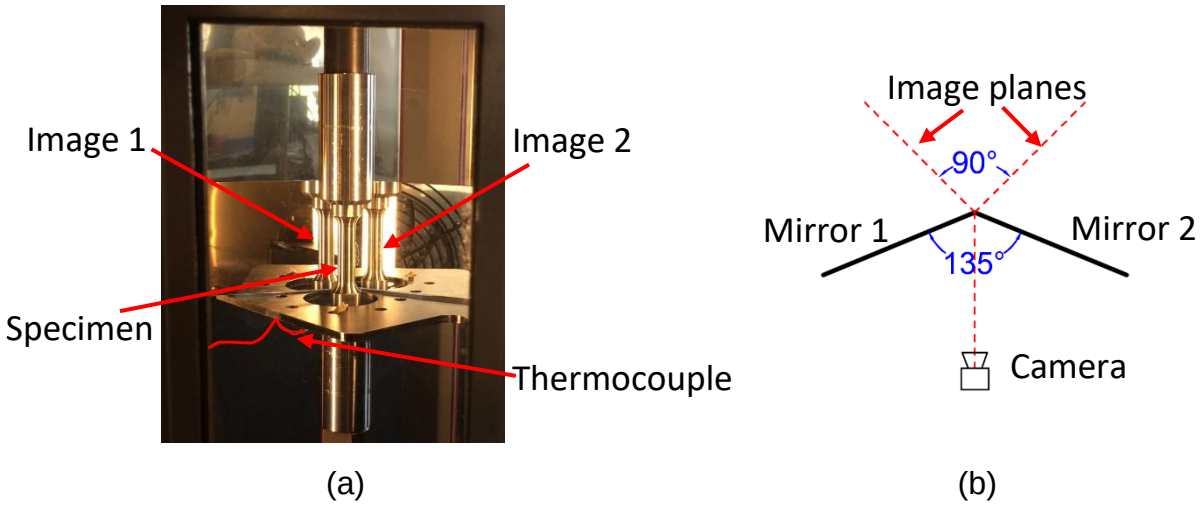

Fig. 3 (a) Layout of the inside of temperature chamber; (b) Illustration of the two-plane mirrors system.

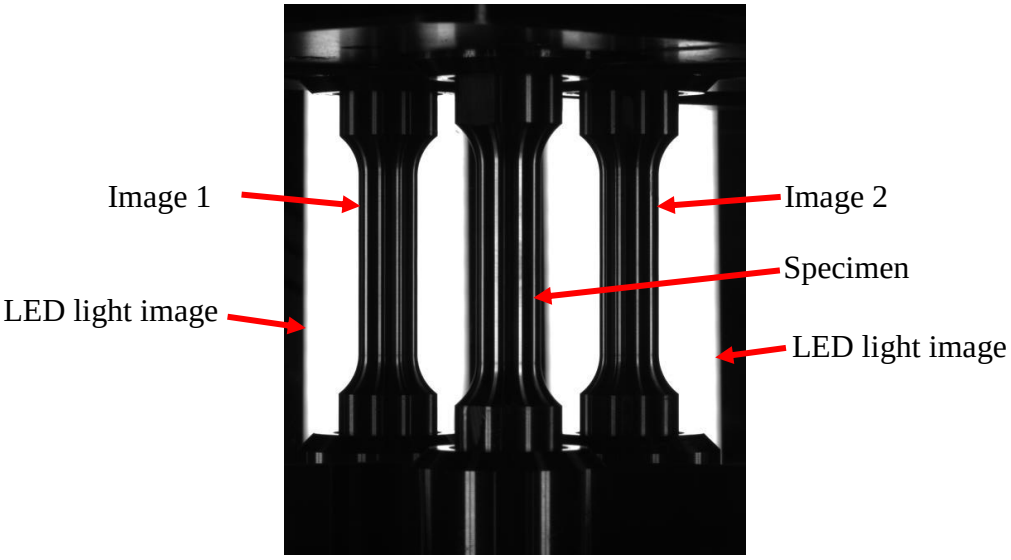

Fig. 4 Picture of smooth round bar specimen taken at the beginning of the test.

2.3 The edge tracing method

Digital pictures consists of numbers of pixels which depend on the resolution of the digital camera [38]. Each pixel in the picture represents a grey-value. From black to white, the grey-value ranges from 0 to 255. Digital pictures can be read by Matlab and grey-value of each pixel can be output and stored in a matrix for analysis. For one arbitrary row in the digital pictures as red line marked in Fig. 5 (a), peak values of the derivative (absolute value) of grey-value can be found, due to the strong contrast between the specimen images and the background, as shown in Fig. 5 (b). There were several peak values in Fig. 5 (b), however, only the two maximum peak values were regarded as the boundaries between the specimen image and the background. The small peak values were caused by the white color on the specimen image, formed due to light reflection. The pixel numbers between the two boundaries represent the corresponding cross-section diameter. By scanning each row of the picture, the edges of the specimen image can be captured, together with the minimum cross-section diameter, shown as red curves in Fig. 6. Due to the existence of necking or notch, the deformation was localized in the necking /notch region. The edge tracing method was therefore mainly focused on the necking/notch region to save calculation cost.

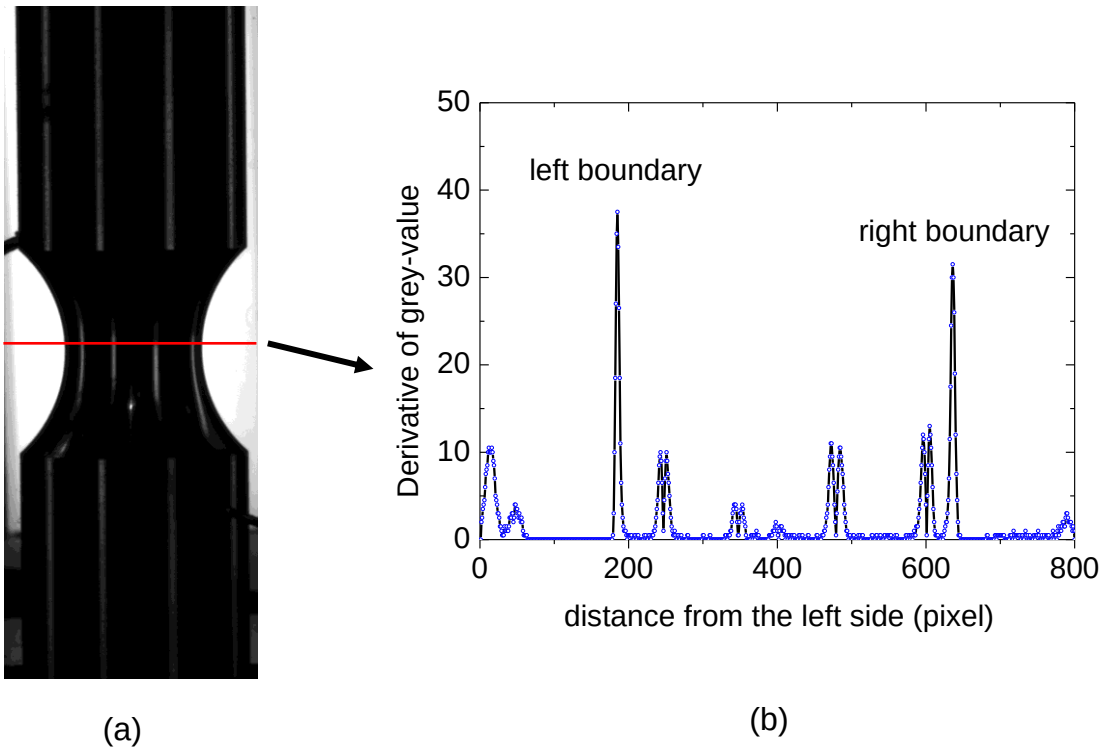

Fig. 5 The edge tracing method. (a) One arbitrary row of pixels of axisymmetric notched specimen with $a_0/R_0 = 0.5$ *; (b) absolute value of derivative of the grey-value.*

Fig. 6 Specimen image edges in Fig. 5 (a) derived with the edge tracing method. The minimum cross-section diameter is also shown in pixels.

Before the test, the minimum cross-section diameter of each specimen was measured with a laser gauge. The 'unit pixel length' then can be calculated by dividing the initial minimum cross-section diameter by the corresponding pixel numbers in the picture taken in the beginning. The current minimum cross-

section diameters are calculated by multiplying the pixel numbers and the 'unit pixel length' in all the following pictures taken during the test. In order to verify the accuracy of the edge tracing method, several trial tests with notched specimens were performed. After certain deformation, we held the test and took a picture of the specimen. Then the minimum cross-section diameter in the same directions as in the picture was measured by the laser gauge. The picture was analyzed with the edge tracing method. The minimum cross-section diameter calculated from the picture agreed well with the value measured by the laser gauge in the same direction, with errors within ± 1.2 %. The trial tests confirmed that the edge tracing method can be used to measure the specimen minimum cross-section diameter accurately. A difference of the minimum cross-section diameters measured in the two perpendicular directions has been observed, from both the edge tracing method and the laser gauge measurement. For example, for the axisymmetric notched specimen with $a_0/R_0 = 0.5$, the minimum cross-section diameters measured were 8.05 and 8.23 mm, at the load $P = 54.33\,KN$. This is attributed to the material anisotropy and anisotropic damage evolution. Therefore, it is more accurate to use the average value of diameters measured in two orthogonal planes in minimum cross-section to characterize the diameter reduction. For all the pictures taken in each test, the edge tracing method was used to detect the specimen image edges and to measure the corresponding average minimum cross-section diameter.

3. Experimental results

In this study, the specimen deformation is characterized by the average true strain ε, which is defined by the minimum cross-section area reduction [39]:

$$\varepsilon = \ln(A_0/A) = 2\ln(a_0/a) \tag{3}$$

where A_0 and A are the initial and current minimum cross-section area, respectively. a is the current averaged minimum cross-section radius measured from the specimen images with the edge tracing method. True stress σ_t for the smooth round bar specimen is calculated by dividing load by the current minimum cross-section area:

$$\sigma_t = P/\pi a^2 \tag{4}$$

Deformed plots of the smooth round bar specimen tested at room temperature and axisymmetric notched specimen with $a_0/R_0 = 0.5$ tested at -60℃ are presented in Fig. 7 and Fig. 8, respectively. For the smooth round bar specimen in Fig. 7, the deformation developed in the whole specimen when the strain is small. As the load increases, diffuse necking occurred, which can be observed on the specimen image in Fig. 7. By studying the specimen images and the load-strain curves, it was found that diffuse necking occurred approximately at the strain $\varepsilon = 0.1$ for tests performed at room temperature. For the smooth specimen tested at low temperatures, the strain corresponding to diffuse necking increased slightly as temperature decreased, seen in Fig. 9 (a). After diffuse necking, the deformation localized in the necking

zone, and a blunt axisymmetric notch was formed. The blunt notch became sharper and sharper, until the specimen failed into two parts. For the axisymmetric notched specimen, deformation localized mainly in the notch region. As the strain increases, the notch deformed form an initial 'U' shape to a 'V' shape, until the specimen failed into two parts, as seen in Fig. 8. For the first picture in which the specimen failure (broken into two parts) was observed in each test, specimen images in the previous frames were used to calculate the strain with the edge tracing method. Note that, in Fig. 7 and Fig. 8, the picture annotated by $\varepsilon = \varepsilon_f$ corresponds to crack initiation, instead of measuring after the complete fracture. This will be discussed in the following section.

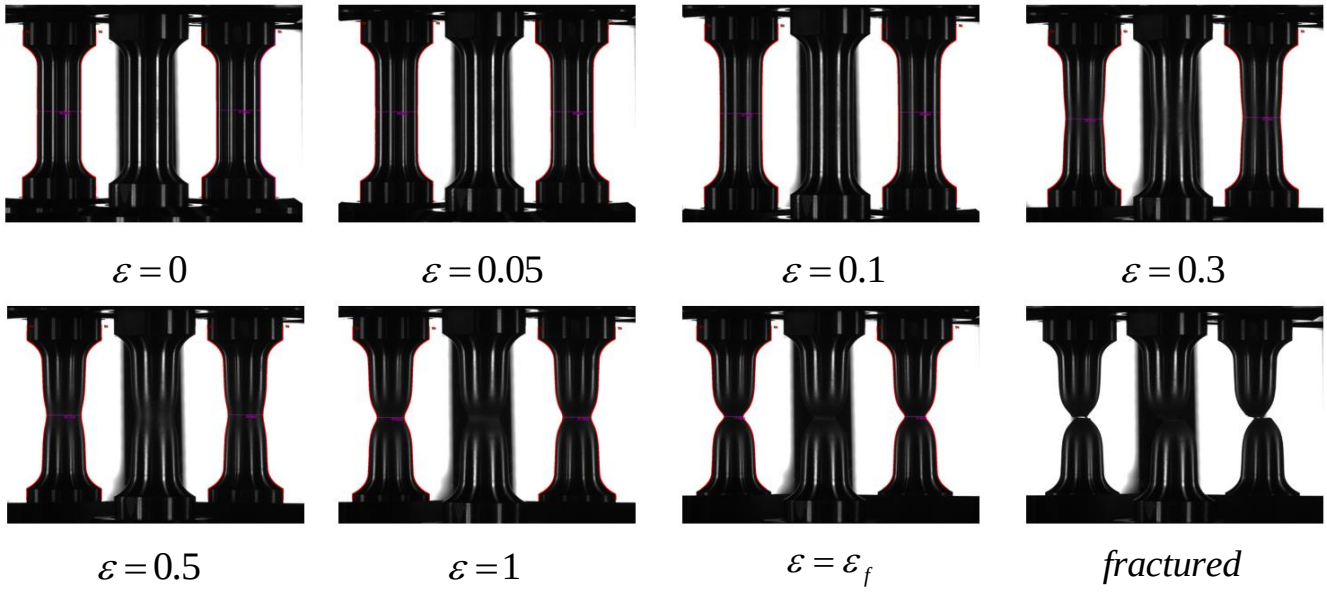

Fig. 7 Smooth specimen at different deformation level tested at room temperature.

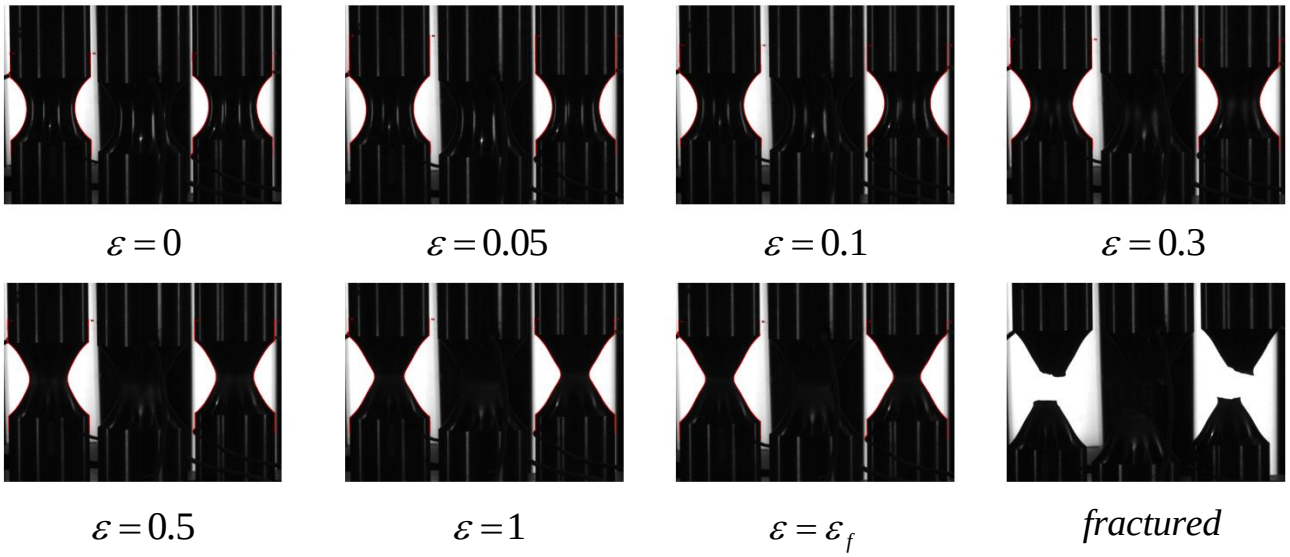

Fig. 8 Axisymmetric notched specimen with $a_0/R_0 = 0.5$ at different deformation levels tested at -60℃.

The load-strain curves and true stress-stain curves of the smooth round bar specimens tested at different temperatures are presented in Fig. 9. As expected, the load increased to a maximum value and then decreased, up to specimen failed. The true stress increases with the decrease of test temperature at the same strain. It can be seen that the maximum load and the strain at the maximum load, $\varepsilon_{P_{\max}}$, increase with the decrease of the test temperature. At the end of the load-strain curves, a sudden drop of load which indicates specimen load carrying capacity loss can be found [13]. This point is regarded as the crack initiation and the corresponding strain is defined as fracture strain, ε_f. It has been pointed out by Benzerga [34] that the strain at crack initiation is smaller than the strain measured from broken specimen fracture surface. The difference is induced due to the server deformation after crack initiation. It is evident in Fig. 9 that the fracture strain ε_f of the smooth round bar specimen increases slightly as temperature decreases. Usually, for most structural steels, decreasing test temperature increases material's strength and hardening, while material's ductility is reduced. Michael and Richard [40] performed quasi-static tensile tests with smooth round bar from 25℃ to 150℃. The specimens were cut from an Al-Cu-Mg-Ag alloy sheet. They found that fracture strain for smooth round bar specimen increased with test temperature increase. Quasi-static tensile test conducted by Børvik and Hopperstad [41] at temperature from 20℃ to 500℃ showed that fracture strain for smooth round bar specimen of Weldox 460 E steel was independent of temperature from 20℃ to 300℃; while from 300℃ to 500℃, fracture strain increased with temperature increase. It is very interesting that the ductility for this 420 MPa structural steel indeed increases (slightly) with decreasing test temperature (down to -60℃). The reason may be that the fracture strain here is defined at crack initiation, instead of strain at the complete fracture of specimens.

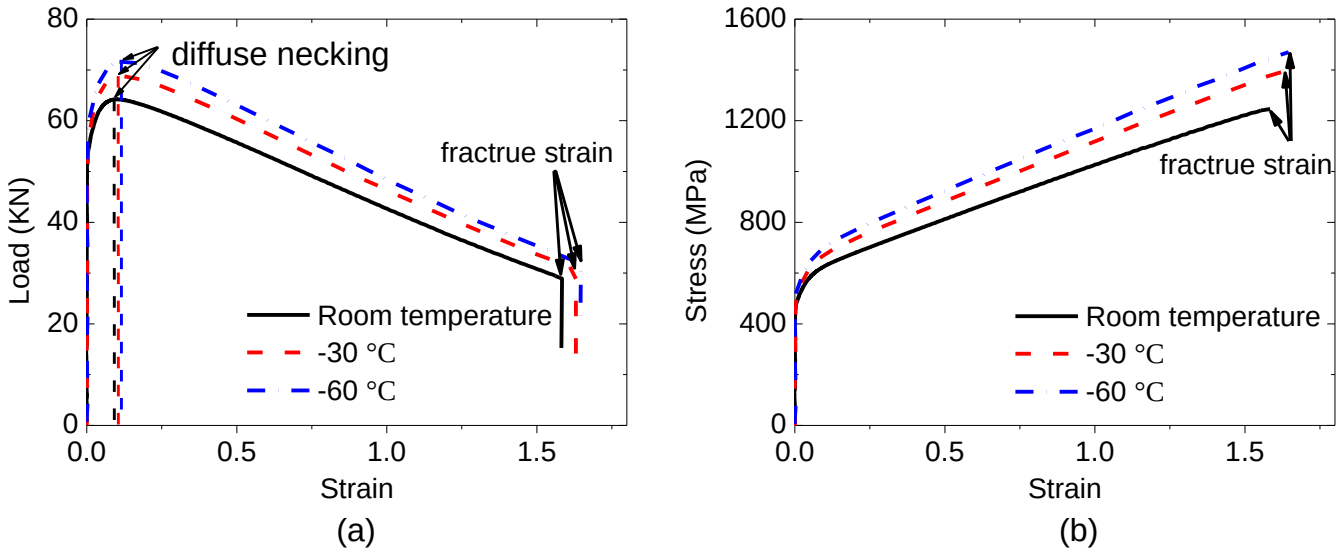

Fig. 9 (a) Load-strain curves of smooth round bar specimen. (b) True stress-strain curves of smooth round bar specimen. The strain corresponding to diffuse necking and fracture are annotated.

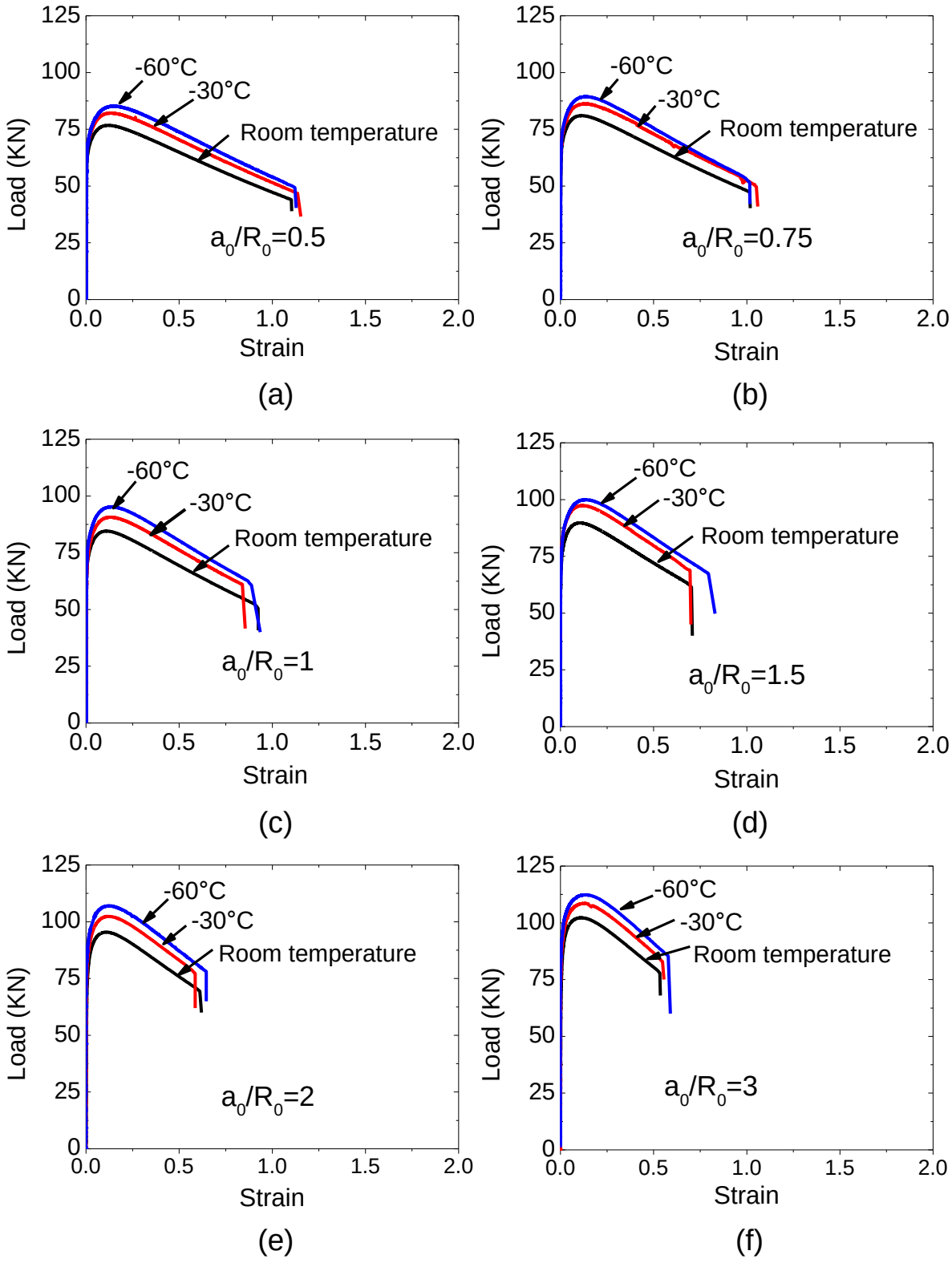

Fig. 10 Load-strain curves for axisymmetric notched tensile specimens with same geometry tested at different temperatures. (a) $a_0/R_0 = 0.5$*; (b)* $a_0/R_0 = 0.75$*;(c)* $a_0/R_0 = 1$*;(d)* $a_0/R_0 = 1.5$*;(e)* $a_0/R_0 = 2$*;(f)* $a_0/R_0 = 3$.

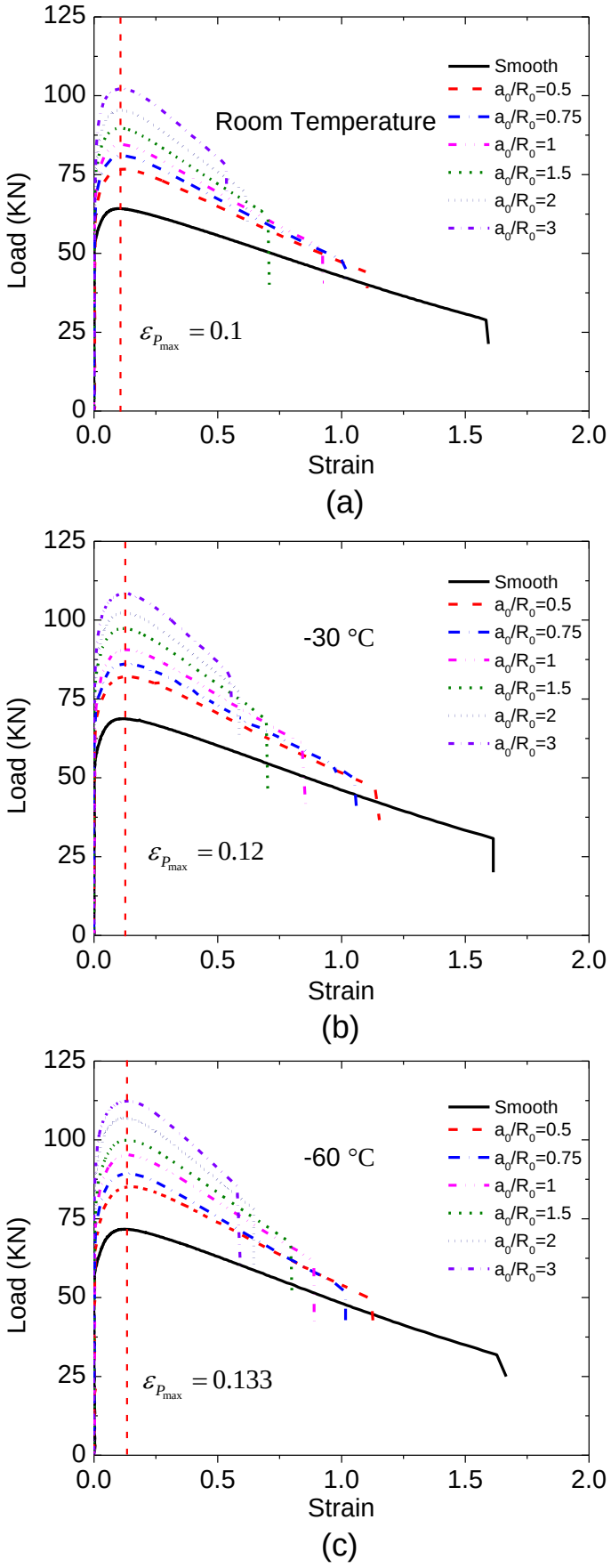

Fig. 11 Load-strain curve for specimens tested at same temperature.

(a) Room temperature; (b) -30℃; (c) -60℃.

Representative load-strain curves for axisymmetric notched specimens with same geometry at different test temperatures are presented in Fig. 10. As expected, the load for specimen tested at lower temperature is larger than that at higher temperature at the same strain level. The maximum load also increases with the decrease of test temperature. The influence of lowering temperature on the fracture strain for each notch geometry shown in Fig. 10 is not very obvious.

Load-strain curves in Fig. 9 and Fig. 10 are regrouped by test temperature and are presented in Fig. 11. It is clearly seen that specimen with sharper notch (larger a_0/R_0) corresponds to higher load at the same strain. The maximum load increases with the increase of a_0/R_0 at each test temperature. Instability analysis of axisymmetric notched tensile specimen showed that the strain corresponding to the maximum load, $\varepsilon_{P_{\max}}$, is a material parameter which is approximately equal to the value of $\varepsilon_{P_{\max}}$ for the smooth round bar specimen and independent of the notch geometry [42]. This is true for the axisymmetric notched specimen tested at the same temperature, as red dash curve points out in Fig. 11. For materials following power law hardening rule, the value of $\varepsilon_{P_{\max}}$ equals to the strain hardening exponent. It should be noted that $\varepsilon_{P_{\max}}$ is sensitive to temperature. For the structural steel studied, $\varepsilon_{P_{\max}}$ increases slightly as temperature decreases.

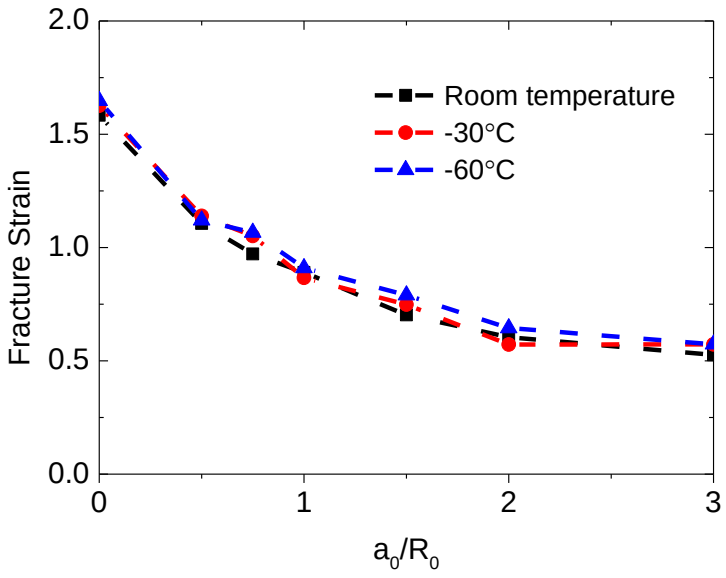

Fig. 12 Fracture strain versus initial notch radius ratio.

The average value of fracture strains from parallel tests in Fig. 11 are presented in Fig. 12 as a function of initial notch radius ratio. It is very interesting to observe that the average fracture strains do not deteriorate with the decrease of temperature to -60℃. For the notched specimens, the fracture strains at low temperatures are somewhat slightly higher than those at room temperature. Michael and Richard [40]

performed quasi-static tensile test with Al-Cu-Mg-Ag alloy from 25℃ to 150℃. They found that the temperature effect on fracture strain for axisymmetric notched specimens can be neglected. Spit Hopkinson tension bar tests at 100 to 500℃ reported by Bøvrik and Hopperstad [18, 36] showed that the influence of test temperature on fracture locus of Weldox 460 E steel was insignificant. Our study in this paper shows that load carrying capacity of smooth and notched specimens of this 420MPa structural steel increase with low temperature, however, the fracture strains (ductility) for smooth and notched specimens don't tend to deteriorate with decreasing test temperature (down to -60℃).

4. Numerical analysis

In order to construct the fracture locus, we need to perform numerical analysis to capture the stress triaxiality evolution. During the loading, the specimen deformed and the stress triaxiality at the center of the specimen minimum cross-section varied accordingly. For non-proportional loading, a strain-weighted average stress triaxiality T^* is widely used [19, 33, 34, 43]:

$$T^* = \frac{1}{\varepsilon_f}\int_0^{\varepsilon_f} T(\varepsilon)\,\mathrm{d}\,\varepsilon \tag{5}$$

In order to capture the evolution of stress triaxiality in the center of minimum cross-section of the necked/notched specimen, we performed numerical analyses with Abaqus/Standard 6.14[44]. The specimen configurations used for numerical analyses are the same as used in experiments. Axisymmetric model is used with very small mesh size (approximately 0.4*0.4 mm) in the notch region. The 4-noded axisymmetric element with reduced integration (CAX4R) is used. Large deformation is accounted. Symmetric boundary condition is applied in the symmetric plane of smooth specimen and axisymmetric notched specimens. A typical mesh of axisymmetric notched specimen with $a_0/R_0 = 3$ is presented in Fig. 13. For all the numerical analyses, the specimen is loaded in displacement control manner.

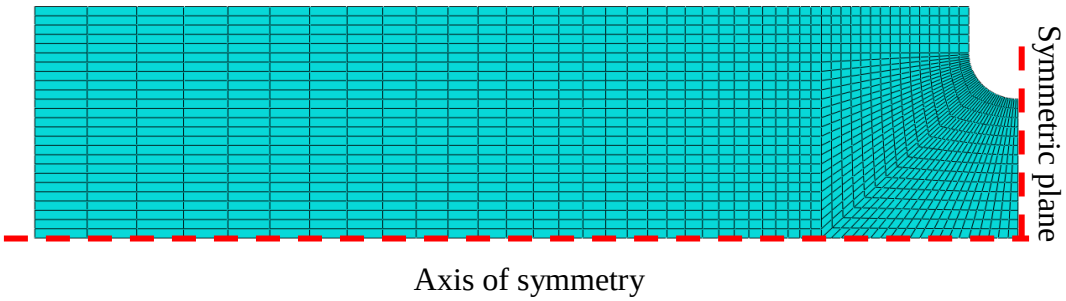

Fig. 13 Typical mesh for axisymmetric notched tensile specimen with $a_0/R_0 = 3$.

The true stress-strain curves in Fig. 9 (b) cannot be used directly for numerical analyses, due to the tri-axial stress state in the specimen necked region after diffuse necking [21, 37, 39, 45]. Bridgman [21] proposed

an analytical correction method based on axisymmetric analysis of a necked round bar specimen, Eq. (6). However, the Bridgman correction is difficult to practice, since the current notch curvature radius should be measured. Le Roy have presented an empirical relation with a/R and ε [46], see Eq. (7). Combined with Eq. (6) and Eq. (7), true stress-strain curves from smooth round bar specimen can be corrected. Fig. 14 shows the equivalent stress-strain curves by correcting the curves in Fig. 9 (b), together with the corresponding true stress-strain curves. Obvious difference can be seen between the true stress-strain curves and equivalent stress-strain curves at large strain. Recently, we proposed a new correction function, with which true stress-strain curve from an axisymmetric notched tensile specimen can be converted to material's equivalent stress-strain curve accurately [47, 48]. The equivalent stress-strain curves derived with notch specimens present to be identical to the Bridgman method for this 420 MPa structure steel. The equivalent stress-strain curves in Fig. 14 are then used in the numerical analyses, together with Poisson ratio $\nu = 0.3$ and Young's modulus $E = 200GPa$.

$$\xi = (1 + \frac{2R}{a}) \cdot \ln(1 + \frac{a}{2R}) \tag{6}$$

$$\frac{a}{R} = 1.1 \cdot (\varepsilon - \varepsilon_{P\max}) \tag{7}$$

$$\sigma_{eq} = \frac{\sigma_t}{\xi} \tag{8}$$

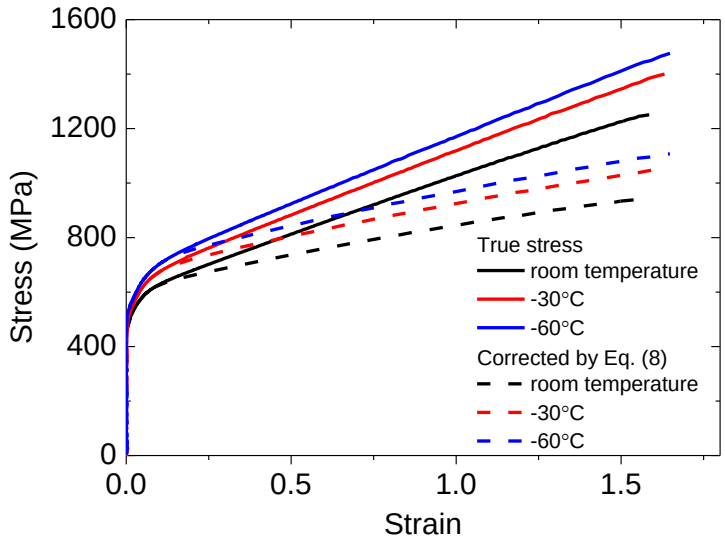

Fig. 14 Equivalent stress-strain curves obtained by correcting true stress-strain curves from smooth specimen at each test temperature with the Bridgman method, Eq. (8).

Load-strain curves from numerical analyses are compared with those from experiments for specimen with same geometry and test temperature. Fig. 15 presents the load-strain curves from experiment and

from numerical simulation for axisymmetric notched specimen with $a_0/R_0 = 2$ tested at -60℃. Very good agreement can be observed, which confirms that the correction function Eq. (8) is accurate. It also indicates that the deformation in the notch region can be well captured during the loading process.

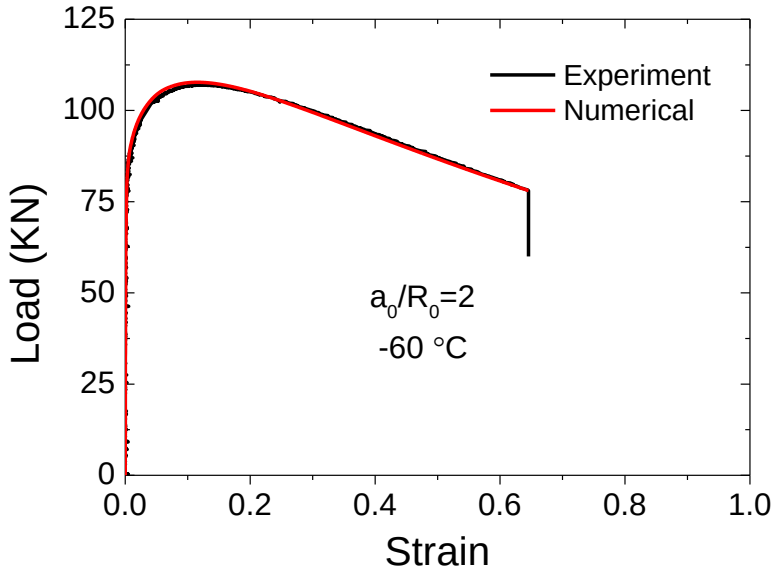

Fig. 15 Comparison of load-strain curves from experiment and from numerical analysis for notched tensile specimen with $a_0/R_0 = 2$ *tested at* -60℃.

From numerical analysis, the stress triaxiality at each material point can be calculated. Fig. 16 presents the stress triaxiality evolution at the center of the minimum cross-section, up to fracture strain. As it can be seen in Fig. 16, for the smooth specimen, the stress triaxiality is constant and equals to 1/3 at the beginning, and then increases with the increase of strain. For axisymmetric notched specimens with $a_0/R_0 \le 1$, stress triaxiality increases with the increase of strain, while for specimens with $a_0/R_0 > 1$, stress triaxiality increases firstly and then decrease with the increase of strain. This infers that the specimen initial notch geometry strongly affects the stress triaxiality evolution. For the smooth specimen, the value of stress triaxiality at fracture presents to be even larger than the notched specimen with $a_0/R_0 = 0.5$ in Fig. 16, reflecting the severe deformation in the necking region at failure for smooth specimen.

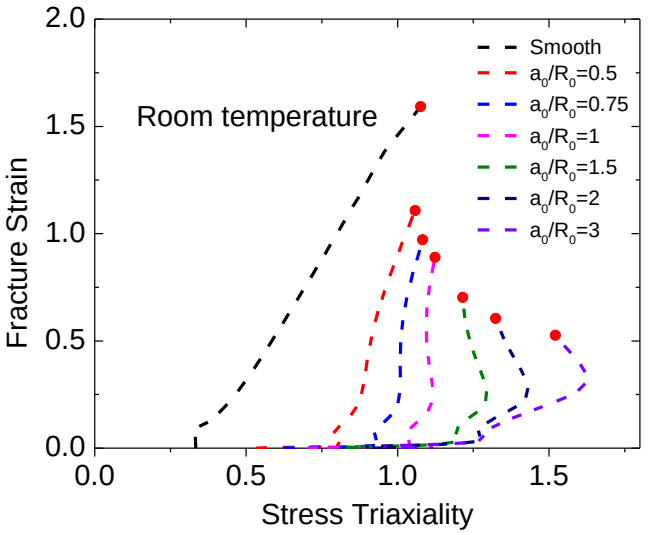

(a)

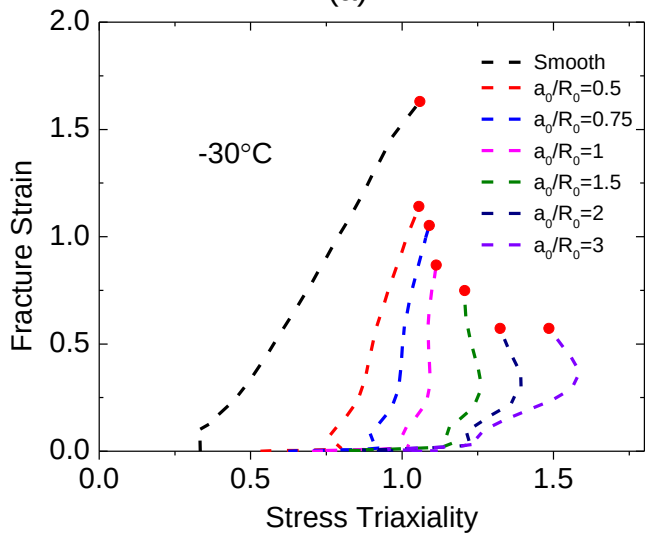

(b)

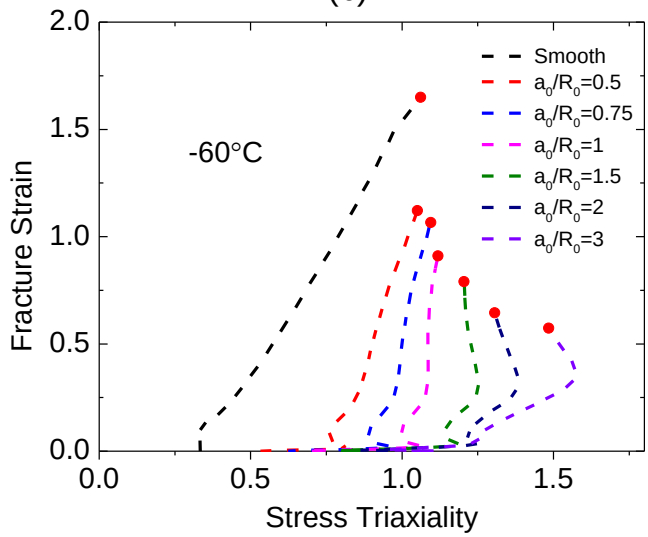

(c)

Fig. 16 Stress triaxiality evolution at the specimen minimum cross-section center up to fracture strain. (a) Room temperature; (b) -30℃; (c) -60℃.

For each specimen in Fig. 16, the average stress triaxiality is calculated by Eq. (5). Fracture strain is plotted against the corresponding average stress triaxiality in Fig. 17 for specimens tested at the same temperature. It can be clearly observed that the fracture strain decreases with the increase of average stress triaxiality. Similar to Fig. 12, the three curves in Fig. 17 almost collapse into one, except small scatter. Interestingly, the local behavior shown in Fig. 17 closely reflect the global behavior in Fig. 12.

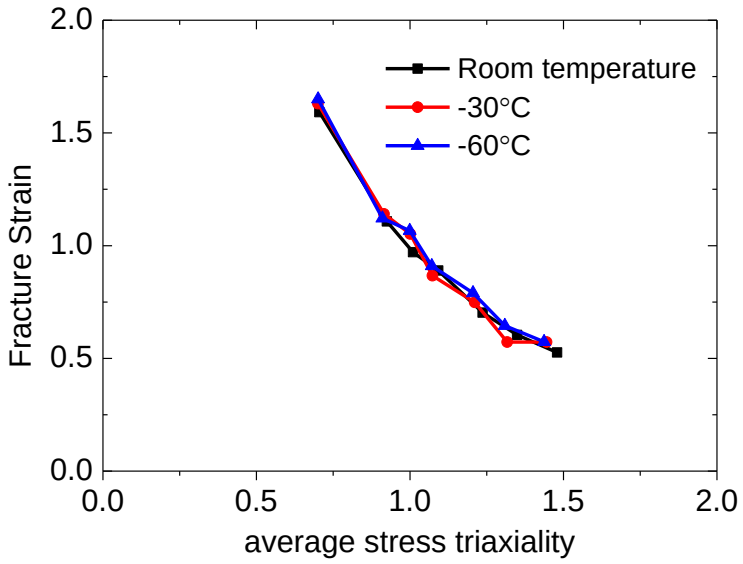

Fig. 17 Fracture strain versus average stress triaxiality at different temperatures.

Indeed, we can formulate the fracture locus with different measures of stress triaxiality: the initial stress triaxiality (calculated by Eq. (1)), the strain-weighted average stress triaxiality and the stress triaxiality at failure. Fig. 18 presents these three measures of fracture loci for specimens tested at room temperature. These three curves behave differently, but show similar trend that the fracture strain decreases with the increase of stress triaxiality. It can be observed that for the smooth specimens, the values of stress triaxiality by different measures differ significantly; while for the notched specimen, the difference tend to decrease with increasing a_0/R_0, especially for the red and green curves. It is difficult to conclude which curve in Fig. 18 is better, since each of them presents pros and cons in certain aspects. For the fracture locus determined with the initial stress triaxiality, it can be conveniently formulated once the fracture strain is known. However, the stress triaxiality evolution or the damage evolution is not considered. The curve constructed on the space of average stress triaxiality and fracture strain takes the strain history into account and depicts the damage accumulation in the form: $D=\int_0^{\varepsilon_f} T(\varepsilon)\, d\varepsilon = T^* \cdot \varepsilon_f$. D is a material failure indicator. However, we need to run numerical analyses in parallel to capture the deformation history and stress triaxiality evolution. The stress triaxiality at failure is more

straightforward to represent the instantaneous stress state at the fracture point. Similar to the strain-weighted average stress triaxiality, numerical analysis is also necessary. Only for proportional loading, fracture loci constructed by initial stress triaxiality, strain-weighted average stress triaxiality and stress triaxiality at failure collapse into one. It should be noted that when it comes to complex or non-proportional loading, the initial and finial value of stress triaxiality are more or less meaningless and the strain-weighted average stress triaxiality tends to be more representative.

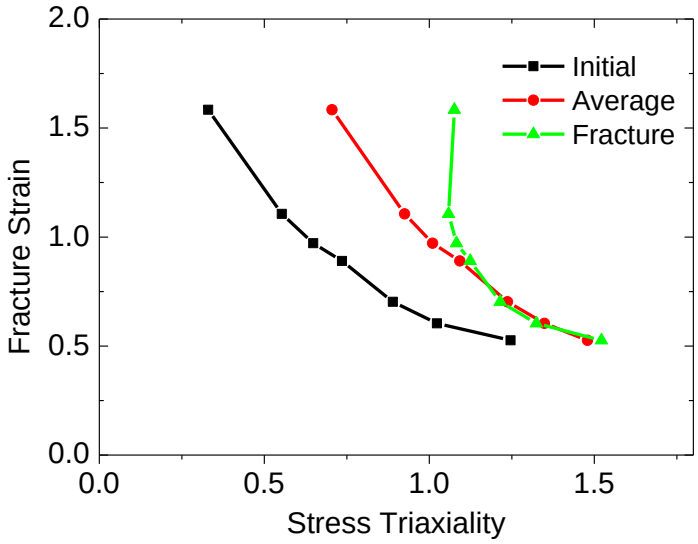

Fig. 18 Fracture strain versus different measures of stress triaxiality for the tests performed at room temperature.

5. Concluding remarks

In this study, smooth round bar specimens and axisymmetric notched tensile specimens have been used to investigate low temperature (down to -60℃) effect on a 420 MPa structural steel fracture locus. A two-plane mirror system and a digital high-speed camera were used together to monitor specimen deformation in the tests. Combined with numerical analyses, the specimen deformation was simulated to capture the stress triaxiality evolution up to failure. Tensile tests with smooth and notched specimen show that decreasing temperature increases material's strength and strain at maximum load, while the fracture strain (ductility) doesn't deteriorate for the testing temperature down to -60℃. The fracture locus formulated with the initial, strain-weighted or the finial value (the value at failure) of stress triaxiality and the fracture strain shows the significant dependence of ductile failure on the stress state. The mechanical response at low temperature in this study indicate that this 420 MPa structural steel is very promising for the application in the Arctic region.

Acknowledgement

The Chinese Scholarship Council is greatly acknowledged for the financial support. The authors wish to thank the Research Council of Norway for funding through the Petromaks 2 Programme, Contract No.228513/E30.

Reference

1. Gautier DL, Bird KJ, Charpentier RR, Grantz A (2009) Assessment of undiscovered oil and gas in the Arctic. *Science*. **324**: 1175-1179.
2. Ren X, Nordhagen HO, Zhang Z (2015) Tensile properties of 420MPa steel at low temperature. *Twenty-fifth Internation Ocean and Polar Engineering Conference*, Hawaii.
3. Tsykahara H, Iung T (1998) Finite element simulation of the Piobert–Lüders behavior in an uniaxial tensile test. *Materials Science and Engineering: A*. **248**: 304-308.
4. Zhang J (2005) Lüders bands propagation of 1045 steel under multiaxial stress state. *International Journal of Plasticity*. **21**: 651-670.
5. Dahl BA (2016) Effect of low temperature tensile priperties on crack driving force for arctic application. *submitted*.
6. Avila JA, Lucon E, Sowards J, Mei PR, Ramirez AJ (2016) Assessment of Ductile-to-Brittle Transition Behavior of Localized Microstructural Regions in a Friction-Stir Welded X80 Pipeline Steel with Miniaturized Charpy V-Notch Testing. *Metallurgical and Materials Transactions A*. **47**: 2855-2865.
7. Capelle J, Furtado J, Azari Z, Jallais S, Pluvinage G (2013) Design based on ductile–brittle transition temperature for API 5L X65 steel used for dense CO2 transport. *Engineering Fracture Mechanics*. **110**: 270-280.
8. Chao YJ, Ward JD, Sands RG (2007) Charpy impact energy, fracture toughness and ductile–brittle transition temperature of dual-phase 590 Steel. *Materials & Design*. **28**: 551-557.
9. Chatterjee A, Chakrabarti D, Moitra A, Mitra R, Bhaduri AK (2015) Effect of deformation temperature on the ductile–brittle transition behavior of a modified 9Cr–1Mo steel. *Materials Science and Engineering: A*. **630**: 58-70.
10. Gopalan A, Samal MK, Chakravartty JK (2015) Fracture toughness evaluation of 20MnMoNi55 pressure vessel steel in the ductile to brittle transition regime: Experiment & numerical simulations. *Journal of Nuclear Materials*. **465**: 424-432.
11. Tanguy B, Besson J, Piques R, Pineau A (2005) Ductile to brittle transition of an A508 steel characterized by Charpy impact test. *Engineering Fracture Mechanics*. **72**: 49-72.
12. Zhang Y, Yu C, Zhou T, et al. (2015) Effects of Ti and a twice-quenching treatment on the microstructure and ductile brittle transition temperature of 9CrWVTiN steels. *Materials & Design*. **88**: 675-682.
13. Bao Y, Wierzbicki T (2004) On fracture locus in the equivalent strain and stress triaxiality space. *International Journal of Mechanical Sciences*. **46**: 81-98.
14. Malcher L, Andrade Pires FM, César de Sá JMA (2014) An extended GTN model for ductile fracture under high and low stress triaxiality. *International Journal of Plasticity*. **54**: 193-228.
15. Mirone G (2007) Role of stress triaxiality in elastoplastic characterization and ductile failure prediction. *Engineering Fracture Mechanics*. **74**: 1203-1221.
16. Mirone G, Corallo D (2010) A local viewpoint for evaluating the influence of stress triaxiality and Lode angle on ductile failure and hardening. *International Journal of Plasticity*. **26**: 348-371.
17. Mohr D, Henn S (2007) Calibration of Stress-triaxiality Dependent Crack Formation Criteria: A New Hybrid Experimental–Numerical Method. *Experimental Mechanics*. **47**: 805-820.
18. Børvik T, Hopperstad OS, Dey S, Pizzinato EV, Langseth M, Albertini C (2005) Strength and ductility of Weldox 460 E steel at high strain rates, elevated temperatures and various stress triaxialities. *Engineering Fracture Mechanics*. **72**: 1071-1087.
19. Yu H, Olsen JS, He J, Zhang Z (2016) Effects of loading path on the fracture loci in a 3D space. *Engineering Fracture Mechanics*. **151**: 22-36.

20. Benzerga AA, Surovik D, Keralavarma SM (2012) On the path-dependence of the fracture locus in ductile materials – Analysis. *International Journal of Plasticity*. **37**: 157-170.

21. Bridgman PW (1952) *Studies in large plastic flow and fracture*. MaGraw-Hill, New York.

22. Johnson GR, Cook WH (1985) Fracture characteristics of three metals subjected to various strains, strain rates, temperatures and pressures. *Engineering Fracture Mechanics*. **21**: 31-48.

23. Peng J, Wu PD, Huang Y, Chen X (2009) Effects of superimposed hydrostatic pressure on fracture in round bars under tension. *International Journal of Solids and Structures*. **46**: 3741-3749.

24. Wu PD, Embury JD, Lloyd DJ, Huang Y, Neale KW (2009) Effects of superimposed hydrostatic pressure on sheet metal formability. *International Journal of Plasticity*. **25**: 1711-1725.

25. Alves Ml, Jones N (1999) Influence of hydrostatic stress on failure of axisymmetric notched specimens. *Journal of the Mechanics and Physics of Solids*. **47**: 643-667.

26. Han KJ, Shuai J, Deng X, Kong L, Zhao X, Sutton M (2014) The effect of constraint on CTOD fracture toughness of API X65 steel. *Engineering Fracture Mechanics*. **124-125**: 167-181.

27. Xu J, Zhang ZL, Østby E, Nyhus B, Sun DB (2010) Constraint effect on the ductile crack growth resistance of circumferentially cracked pipes. *Engineering Fracture Mechanics*. **77**: 671-684.

28. Z.L.Zhang, Niemi E (1994) Studies on the ductility predictions by different local failure criteria. *Engineering Fracture Mechanics*. **48**: 529-540.

29. Dunand M, Mohr D (2011) On the predictive capabilities of the shear modified Gurson and the modified Mohr–Coulomb fracture models over a wide range of stress triaxialities and Lode angles. *Journal of the Mechanics and Physics of Solids*. **59**: 1374-1394.

30. Dunand M, Mohr D (2014) Effect of Lode parameter on plastic flow localization after proportional loading at low stress triaxialities. *Journal of the Mechanics and Physics of Solids*. **66**: 133-153.

31. Bryhni Dæhli LE, Børvik T, Hopperstad OS (2016) Influence of loading path on ductile fracture of tensile specimens made from aluminium alloys. *International Journal of Solids and Structures*. **88-89**: 17-34.

32. Mohr D, Marcadet SJ (2015) Micromechanically-motivated phenomenological Hosford–Coulomb model for predicting ductile fracture initiation at low stress triaxialities. *International Journal of Solids and Structures*. **67-68**: 40-55.

33. Bai Y, Teng X, Wierzbicki T (2009) On the Application of Stress triaxiality formula for plane strain fracture testing. *Journal of Engineering Material and Technology*. **131**.

34. Basu S, Benzerga AA (2015) On the path-dependence of the fracture locus in ductile materials: Experiments. *International Journal of Solids and Structures*. **71**: 79-90.

35. Børvik T, Hopperstad OS, Berstad T (2003) On the influence of stress triaxiality and strain rate on the behaviour of a structural steel. Part II. Numerical study. *European Journal of Mechanics - A/Solids*. **22**: 15-32.

36. Hopperstad OS, Børvik T, Langseth M, Labibes K, Albertini C (2003) On the influence of stress triaxiality and strain rate on the behaviour of a structural steel. Part I. Experiments. *European Journal of Mechanics - A/Solids*. **22**: 1-13.

37. Bao Y, Wierzbicki T (2005) On the cut-off value of negative triaxiality for fracture. *Engineering Fracture Mechanics*. **72**: 1049-1069.

38. Bruck HA, McNeill SR, Sutton MA, Peters WH (1989) Digital image correlation using Newton-Raphson method of partial differential correction. *Experimental Mechanics*. **29**: 261-267.

39. Tu S, Ren X, Nyhus B, Akselsen OM, He J, Zhang Z (2017) A special notched tensile specimen to determine the flow stress-strain curve of hardening materials without applying the Bridgman correction. *Engineering Fracture Mechanics*. **179**: 225-239.

40. Michael JH, Richard PG (1997) Elevated temperature fractrue toughness of Al-Cu-Mg-Ag sheet Characterization and modeling. *Metallurgical and Materials Transactions A*. **28A**: 1815-1829.

41. Børvik T, Hopperstad OS, Berstad T, Langseth M (2001) A computational model of viscoplasticity and ductile damage for impact and penetration. *European Journal of Mechanics - A/Solids*. **20**: 685-712.

42. Zhang ZL, Hauge M, Thaulow C, Ødegård J (2002) A notched cross weld tensile testing method for determining true stress–strain curves for weldments. *Engineering Fracture Mechanics*. **69**: 353-366.

43. Bao Y, Wierzbicki T (2004) A Comparative Study on Various Ductile Crack Formation Criteria. *Journal of Engineering Materials and technology*. **126**: 314-324.

44. Abaqus (2014) *Abaqus User Manual (Version 6.14)*.

45. Mirone G (2004) A new model for the elastoplastic characterization and the stress–strain determination on the necking section of a tensile specimen. *International Journal of Solids and Structures*. **41**: 3545-3564.

46. Roy GL, Embury JD, Edward G, Ashby MF (1981) A model of ductile fracture based on the nucleation and growth of voids. *Acta Metallurgica*. **29**: 1509-1522.

47. Tu S, Ren X, He J, Zhang Z (2018) A method for determining material's equivalent stress-strain curve with any axisymmetric notched tensile specimens without Bridgman correction. *International Journal of Mechanical Sciences*. **135**: 656-667.

48. Tu S, Ren X, He J, Zhang Z Experimental measurement of equivalent stress-strain curve of a 420 MPa structure steel with axisymmetric notched tensile specimen. *In preparation*.